Modulating the Cavity Size of Carbon Nanobelts for Enhanced Oxygen Reduction Reaction

Tingting Xu,[b] Xiaofei Zhang,[a]* Zao Wang,[d] Pei Wen Ng,[b] Liuying Jiao,[b] Shi-Qiang Wang,[a] Khoong Hong Khoo,[c] Zhengtao Xu,[a] Jishan Wu,[b] Jun Zhu[a]*

a. Institute of Materials Research and Engineering (IMRE), Agency for Science, Technology and Research (A*STAR), 2 Fusionopolis Way, Singapore 138634

b. Department of Chemistry, National University of Singapore, 3 Science Drive 3,117543, Singapore

c. Institute of High Performance Computing (IHPC), Agency for Science, Technology and Research (A*STAR), 2 Fusionopolis Way, Singapore 138634

d. State Key Laboratory of Transient Chemical Effects and Control, Shannxi Applied Physics-Chemistry Research Institute, Xi'an 710061, Shannxi, China

ABSTRACT: The pre-activation of reactants within the cavities of carbon nanotubular materials has remained largely unexplored due to the scarcity of materials with well-defined sizes and precisely engineered doping sites. Herein, we demonstrate that the catalytic activity toward oxygen reduction reaction (ORR) is primarily governed by the cavity sizes of well-defined nanobelt materials with precisely doped sp^2-nitrogen atoms. Our results show that the confinement effect induced by cavity size and the electron-rich chemical environment within the cavity are crucial for O_2 adsorption and pre-activation, leading to enhanced catalytic activity. **Belt2**, with its medium-sized cavity (6.3 Å), exhibits superior ORR catalytic performance compared to **Belt1** with its narrower cavity and **Belt3**/**Belt4** with their larger cavities. Notably, **Belt2** achieves high half-wave and onset potentials of 0.84 and 0.97 V, respectively, along with an open circuit voltage of 1.32 V and a peak power density of 181 mW cm^{-2} in a zinc-air battery. This work not only provides a deeper understanding of the geometric factors influencing ORR electrocatalysis of nanocarbon materials but also offers insights into the future design of nanocarbon electrocatalysts for enhancing catalytic efficiency. These findings may also be beneficial for other energy conversion and catalytic materials.

INTRODUCTION

The oxygen reduction reaction (ORR), which serves as the cathodic reaction in fuel cells and metal-air batteries, holds a crucial role in the field of energy conversion research and fundamental electrochemistry.[1-3] Over the past decade, extensive research has focused on the development of various metal-free carbon-based materials as promising catalysts to replace the current high-cost and less durable platinum-based materials for the large-scale commercialization of this technology,[4-6] including carbon nanotubes (CNTs),[7, 8] graphene/graphite,[9-11] carbon nitride[12, 13] and covalent organic frameworks (COFs)[14-16].

The arrangement of catalytic active sites within specific geometric structures is crucial for optimizing catalytic efficiency and selectivity.[17-22] While typical ORR catalysts often feature active sites situated on material surfaces for surface catalysis, it is usually accompanied by the occurrence of competing side reactions due to the lack of sufficient stabilization and activation for specific reactants and intermediates. On the contrary, space confined catalysts with active particles/dopants anchored within specific spaces have been developed for enhanced catalytic activity and selectivity, though their inherent shortcomings, including ambiguously defined active sites and difficulties in precise synthesis, make it challenging to systematically study their intrinsic activities and greatly limit their potential applications (Figure 1).

The extensively studied ORR catalysts, CNTs, are unique for their radially oriented π-orbitals and strained nanotubular structures, which can induce confinement effect in catalysis.[23, 24] The inherent rigidity of these nanotubular structures confines the size of encapsulated materials and facilitates interactions between the encapsulated molecules and the interior surfaces of the CNTs. Additionally, the curvature of the CNT walls induces a shift in π-electron density from the concave interior to the convex exterior, resulting in an electric potential difference.[25-27] These attributes collectively position CNTs as promising candidates for electrocata-

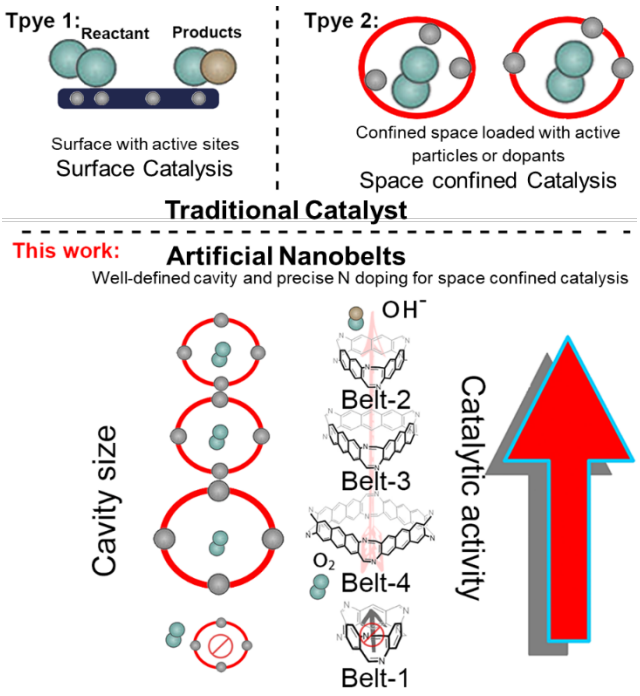

Figure 1. Traditional surface and space confined catalysis, and the designed artificial nanobelts for confined catalysis in this work.

lytic materials.[28-30] As research endeavours intensified, it became evident that introducing heteroatoms into CNTs could significantly enhance their catalytic activity for ORR.[31-33] However, impurities resulted from the synthetic process usually necessitate further purification, and geometric defects can also have a significant impact on catalytic activity compared to intact structures.[34] Another concern arises from the fact that the prepared CNTs usually form a blend of single-walled and multi-walled CNTs with non-uniform cavity sizes, lengths and ambiguously defined doping sites. Consequently, the systematic investigation of their catalytic performance in relation to these geometric features remains challenging and largely unexplored.

Organic synthesis offers a reliable and promising alternative approach for the preparation of CNTs and CNT analogues with uniform and precisely defined structures.[35] Despite being in its infancy, significant progress has been made in the synthesis of challenging molecular carbon nanobelts (CNBs), which represent the simplest fragments of CNTs.[36] They can serve as effective models for systematic study of the properties and applications corresponding to the nanotubular materials with comparable cavity sizes. However, most of them are pure carbon materials and there is lack of available sp^2-nitrogen-doped CNBs materials for investigating the influence of cavity sizes on their catalytic activity. Herein, we prepared a series of precisely engineered sp^2-nitrogen-doped CNBs with varying sizes by following our previously reported strategy, [37, 38] and revealed their cavity-size-dependent ORR catalytic activity (Figure 1). Our results illustrated the substantial influence of the cavity-size-induced confinement effect and electron-rich cavity chemical environment on the ORR catalytic activity of nanocarbon materials. Notably, CNBs with a cavity diameter of about 6.3 Å exhibited higher ORR efficiency, with high half-wave and onset potentials of 0.84 and 0.97 V, respectively. Moreover, investigating the materials as cathode electrocatalyst in a zinc-air battery exhibited a high open circuit voltage of 1.32 V and peak power density of 181 mW cm^{-2}. Overall, this work not only contributes to a better understanding of the geometric factors influencing ORR electrocatalysis of nanocarbon materials but also provides insights for the future deign and optimization of carbon nanomaterials with respect to their cavity size for the enhancement of catalytic efficiency.

RESULTS AND DISCUSSION

The preparation of CNBs, **Belt1**, **Belt2**, **Belt3** and **Belt4**, followed our previous report with some modifications (Scheme 1a-c). [37, 38] Refluxing the respective precursors, **P1**, **P2** and **P3**, in toluene or *o*-dichlorobenzene (*o*-DCB) with diphenyl phosphate as the acid catalyst yielded four nitrogen-doped CNBs with varying sizes. Subsequently, the CNBs were recrystallized by slow diffusion of methanol into their respective saturated dichloromethane (DCM) solutions to afford crystalline materials. The CNBs exhibit conjugated backbone structures with sp^2-nitrogen atoms precisely doped in the tub-shaped eight-membered rings (also known as 1,5-diazocine). Unlike Schiff base C=N bonds, the C=N bonds in the eight-membered 1,5-diazocine rings maintain a good degree of backbone conjugation and display excellent stability.[39] Structures of **Belt1** and **Belt2** were resolved by X-ray crystallographic analysis of their single crystals (Figure S1) while diffraction signals of the single crystals of **Belt3** and **Belt4** were too weak to be resolved. Nevertheless, their structures are sufficiently evidenced by mass spectroscopy, ^{1}H and ^{13}C NMR spectroscopy and theoretical calculation. X-ray crystallographic analysis revealed that the belt-shaped molecules pack into 1D channels by intermolecular [C-H···π] and van der Waals

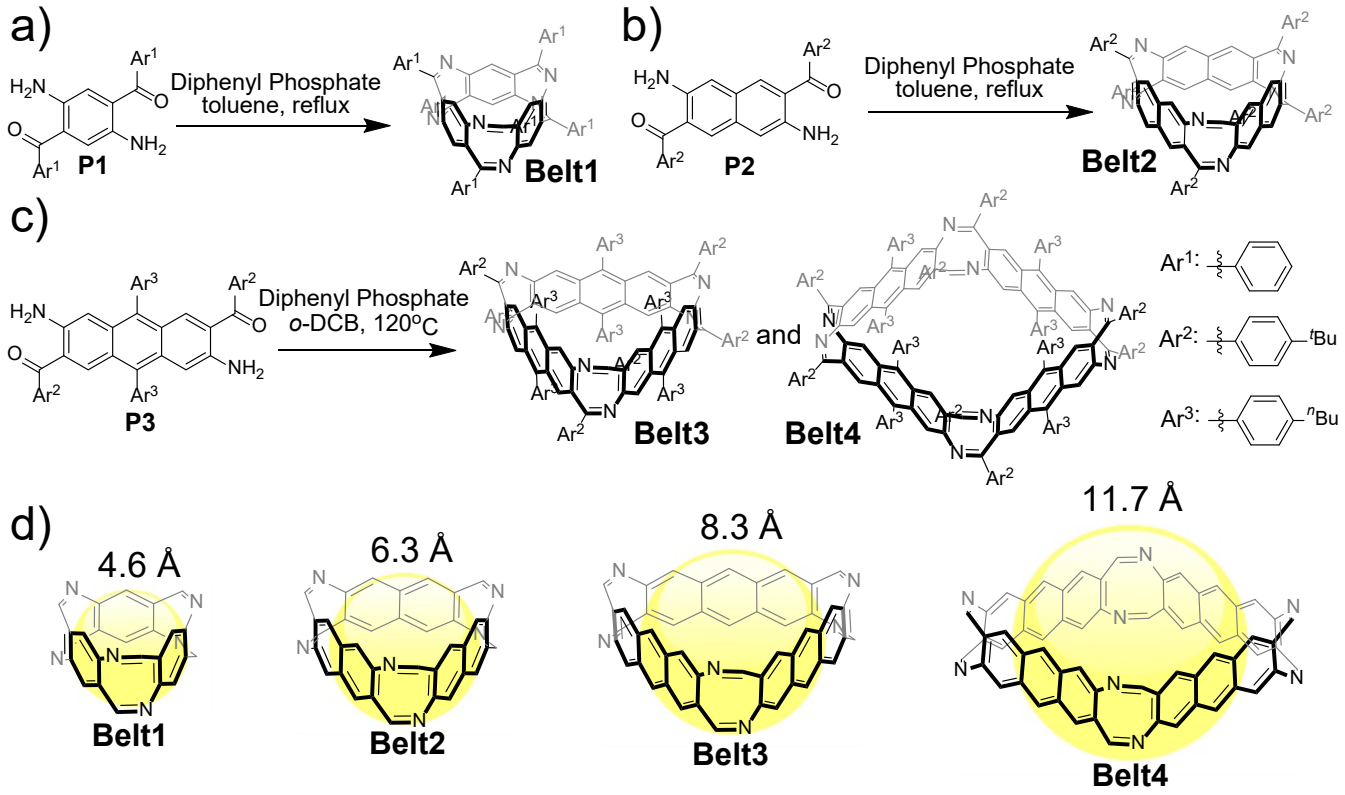

Scheme 1. a)-c) Synthesis of **Belt1-4**; d) Comparison of the cavity sizes of **Belt1-4** (Substituents and hydrogens are omitted for clarity).

interactions, forming supramolecular nanotube structures in the solid states (Figure S1a-d). The channel sizes of **Belt1** and **Belt2** were determined to be 4.6 Å and 6.3 Å by X-ray crystallographic analysis (in line with theoretically calculated sizes), and it is 8.3 Å for **Belt3** and 11.7 Å for **Belt4** based on their optimized structures (Scheme 1d and Figure S1e).

10 wt% of carbon black was added and grinded together with the afforded CNBs materials to improve both their conductivity and compatibility with aqueous electrolyte during the investigation of their ORR activities. Their linear sweep voltammetry (LSV) curves were obtained at different rotation rates (400 to 2500 rpm) in oxygen-saturated 0.1 M KOH aqueous electrolyte (Figure S2-5). Besides, LSV curves of carbon black and commercial 20 wt% Pt/C catalysts were also measured for comparison. The ORR half-wave and onset potentials of **Belt1-4**, carbon black and Pt/C were determined to be 0.76/0.87, 0.84/0.97, 0.81/0.94, 0.80/0.94, 0.59/0.70 and 0.86/1.01 V (vs. RHE), respectively, from their LSV curves measured at 1600 rpm (Figure 2a and 2b). In general, both the half-wave and onset potentials of belt materials are more positive than that of carbon black, and they are only considerably smaller than that of commercial Pt/C, illustrating their excellent ORR activity as metal-free catalysts (comparing to various state-of-the-art ORR metal-free catalysts, Table S1). Among **Belt1-4**, the more positive half-wave and onset potential of **Belt2** (0.84/0.97 V) indicated its more efficient ORR activity, followed by **Belt3**, **Belt4** and **Belt1**. The corresponding electron transfer number (n) of **Belt1-4** extracted from Koutecky-Levich (K-L) plots at different potentials were 3.87, 3.97, 3.95, and 3.95, respectively (Figure S6-9), clearly indicating a $4e^-$ transfer pathway in the ORR process (The electron transfer numbers were consistent with the values determined by RRDE measurements, Figure S10 and S11). The Tafel slopes derived from LSV curves were 74.8, 49.5, 56.5 and 62.2 mV dec^{-1}, respectively for **Belt1-4** (Figure 2c). The smaller Tafel slope of **Belt2** (49.5 mV dec^{-1}), again, indicated its faster ORR reaction kinetics.

The electrochemical active surface areas (ECSAs) of **Belt1-4** were estimated by measurement of the electrochemical double layer capacitance (C_{dl}) using the cyclic voltammetry method (change in current density vs. scan rate). The ECSAs of **Belt1-4** were determined to be 2.3, 3.7, 4.4, 5.1 mF cm^{-2},

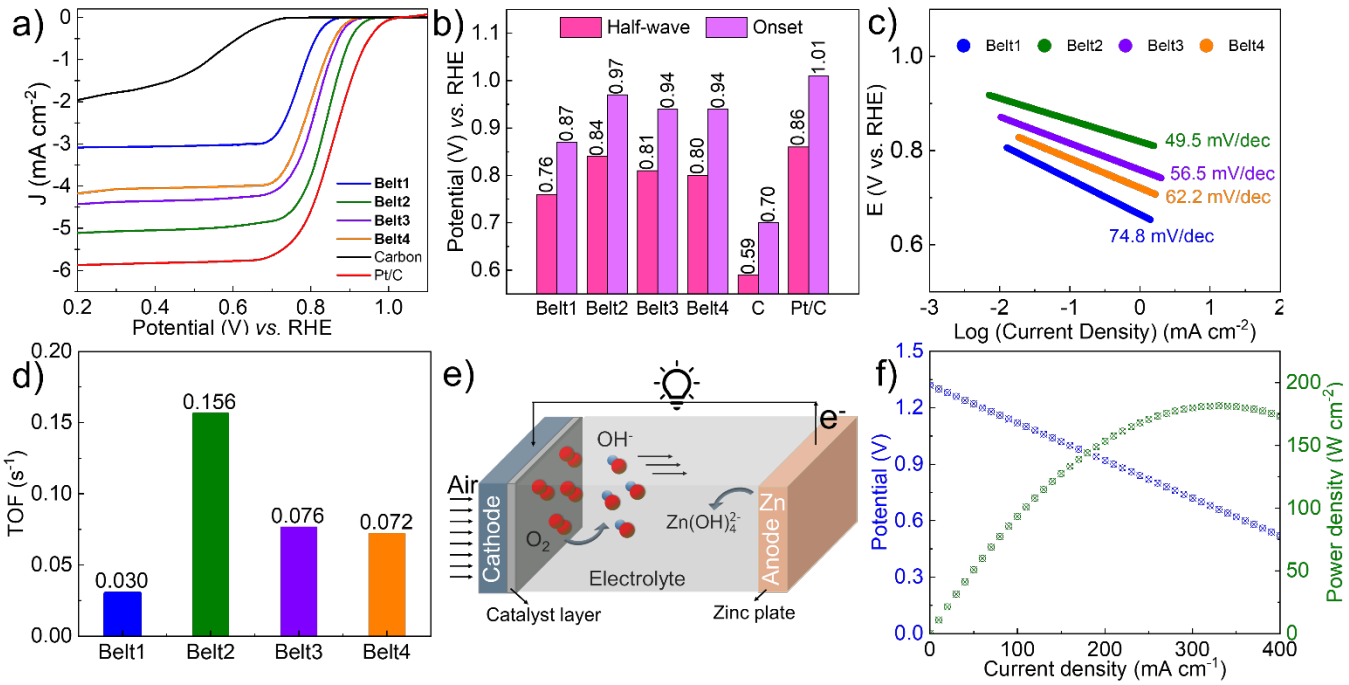

Figure 2. (a) LSV curves (at 1600 rpm) of carbon black (black), Pt/C (red) and **Belt1-4** (blue, green, purple and orange) in O_2-saturated 0.1 M KOH electrolyte; (b) Comparison of their half-wave and onset ORR potentials; (c) Comparison of their Tafel plots; (d) Comparison of their TOFs; e) The schematic representation of a Zn-air battery; f) The charge polarization and power density curves of the Zn-air battery using **Belt2** as the cathode electrocatalyst layer.

respectively (Figure S12-15). The ECSAs shows a positive correlation with increasing cavity sizes of the belt materials. Nonetheless, **Belt2** has a smaller electrochemically active surface area as compared to that of **Belt3** and **Belt4**, but exhibits better ORR performance regarding to the halfwave and onset potentials, current densities and Tafel slopes, which implies **Belt2** should possess a higher active site utilization efficiency. Subsequently, the turnover frequencies (TOFs) were calculated at 0.7 V vs. RHE to evaluate the intrinsic activities of **Belt1-4**.[5, 6] The TOFs of **Belt1-4** were estimated to be 0.030, 0.156, 0.076, and 0.072 s^{-1}, respectively (Figure 2d). The larger TOF value of **Belt2** indicates its higher active sites utilization efficiency, followed by **Belt3**, **Belt4** and **Belt1**. The durability of **Belt1-4** was evaluated at 0.7 V vs. RHE for 50000 s. A low current density loss (about 5%) was observed for all belt materials (Figure S16), suggesting their good stability in alkaline condition. Besides, the current densities were largely retained upon addition of methanol into the electrolyte solution at 20000 s (Figure S17), indicating their excellent tolerance towards small organic molecules. Considering the excellent catalytic performance of **Belt2** in ORR process, its application potential was further investigated in an aqueous zinc-air battery (Figure 2e). It can be observed that approximately 98% of the initial voltage was maintained after being discharged for 18 h (Figure S18). The battery demonstrated a high open circuit voltage of 1.32 V and a peak power density of 181 mW cm^{-2} (Figure 2f), indicating its excellent performance as a cathode electrocatalytic material and great potential in energy conversion applications.

To address the differences in ORR activity of **Belt1-4**, their nitrogen contents were investigated since some previous studies have demonstrated a positive correlation between the nitrogen contents doped in the materials and ORR catalytic activity.[40, 41] The nitrogen contents for **Belt1-4** were determined to be 9.98%, 6.32%, 3.70% and 3.70%, respectively. Obviously, although **Belt1** possesses the highest nitrogen content, yet it exhibits the poorest ORR catalytic activity, which suggests that the catalytic differences cannot be explained by their nitrogen contents. As depicted in Scheme 1d, these belt materials have similar molecular structures, same type of heteroatom doping and doping sites as well as similar skeleton electronic properties. Intuitively, their obvious difference in cavity sizes could be responsible for the variations in ORR activities. From atomic-level analysis, these nanobelts with tunable cavity sizes

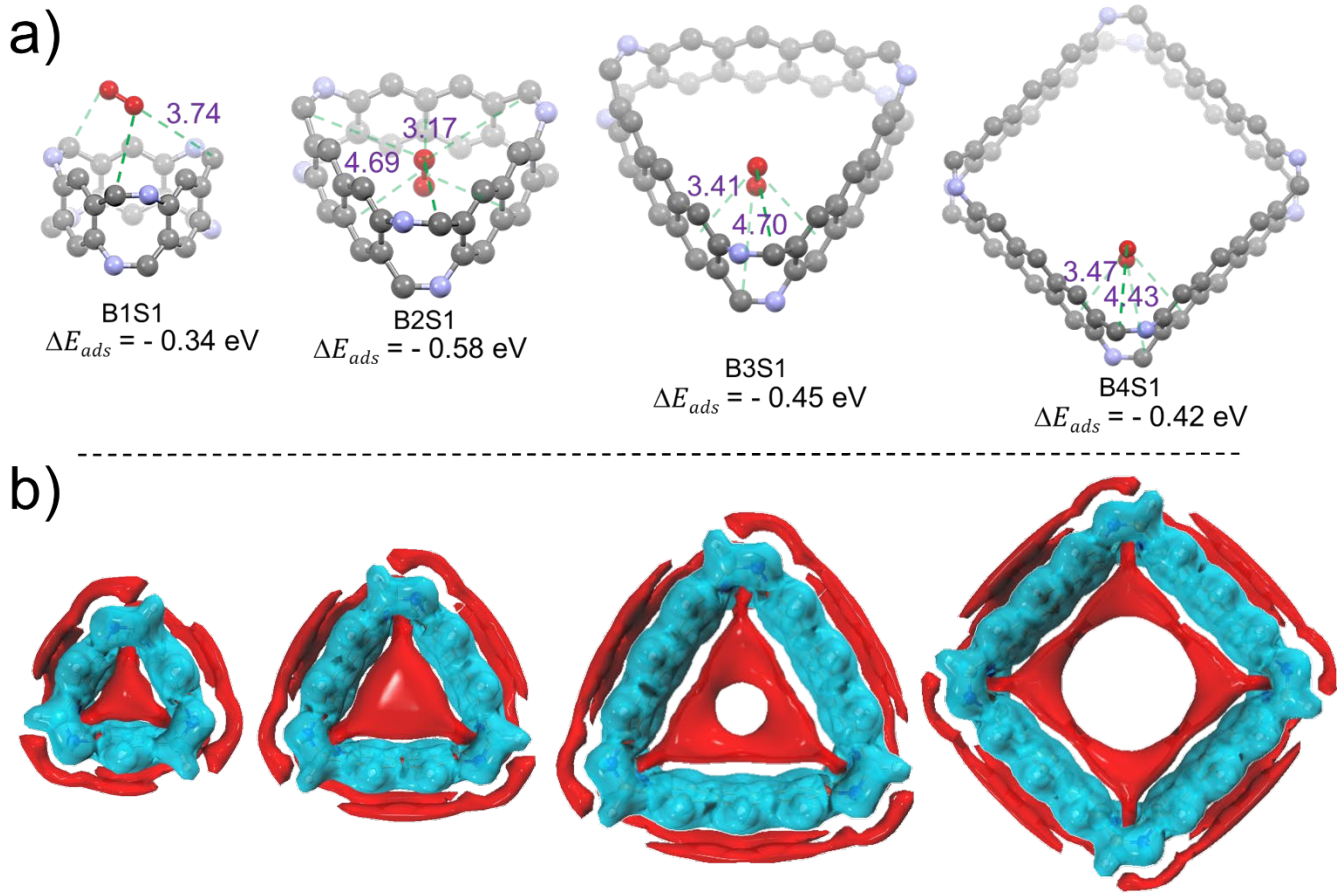

Figure 3. a) The most favorable O2 adsorption configurations for **Belt1-4** determined by DFT calculations (substituents and hydrogens are omitted for clarity); b) The calculated electron density isosurfaces for **Belt1-4** (isovalues: -2.0 for red, electron rich region; +6.0 for cyan, electron deficient region).

and radially arrayed π-electrons can exhibit a confinement effect within the cavities, which offers additional opportunities to enhance the catalytic activity and selectivity for specific products compared to 2D materials. However, when the cavity size increases beyond a certain diameter, the confinement effect would become less significant as illustrated in some theoretical studies.[42-44] Eventually, the interior and exterior surfaces would behave like 2D carbons at micro-level for tubes with very large diameters. Therefore, the noticeable differences in catalytic activity of **Belt1-4** inspired us to explore the underlying causes through both theoretical calculation and experimental validation.

Characterized by the precise nitrogen doping sites and tunable cavity sizes, these well-defined belt materials provide atomic-level insights into the intrinsic relationship between structures and ORR catalytic activity. Firstly, the electrostatic potential (ESP) surfaces of molecular oxygen and **Belt1-4** were disclosed at the M06-2X/6-311G level (Figure S19) for the identification of possible O_2 binding sites. The nitrogen atoms in **Belt1-4** possess a strong negative electrostatic potential due to high electronegativity, causing the nearby carbon atoms to be more electrostatically positive (C=N and C-N). Therefore, these nearby carbon sites could be possible active sites for ORR. Hirshfeld atomic charges suggested that ORR occurs more favorably at C_3 (in C=N) rather than C2 (in C-N) due to its higher atomic charge for stronger O_2 affinity (Figure S20).

Considering the only slight charge difference of C3 sites in **Belt1-4**, we further explored the effects of their cavity sizes on catalytic activity. DFT calculations for the adsorption models of oxygen in belt cavities were then performed to identify the optimal adsorption site and configuration for O_2. The most favorable configuration, denoted as B1S1 (Figure S21), shows O_2 residing above the cavity of **Belt1** (ΔE_{ads} = -0.34 eV), with van der Waals interactions between the oxygen atoms and the C3 carbon atoms (van der Waals distance, d_{vdw} = 3.74 Å). The

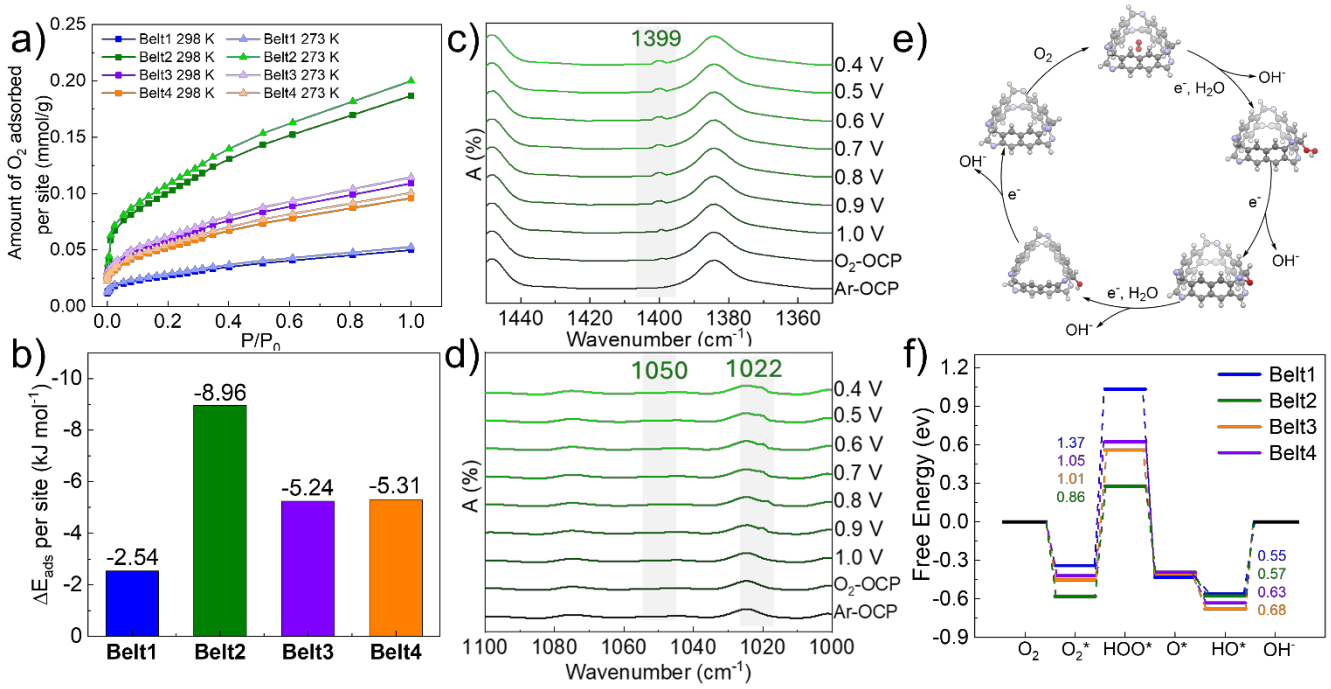

Figure 4. a) The oxygen adsorption isotherm of **Belt1-4** at 273 K and 298 K; b) The calculated isosteric heat of adsorption per site for **Belt1-4**; c) d) The in situ electrochemical ATR-FTIR spectra of **Belt2** measured in 0.1 M KOH electrolyte from 1.0 V to 0.4 V (vs RHE); The spectra in Argon- and Oxygen-saturated electrolyte at open circuit potential (OCP) were also obtained for comparison; e) The proposed 4e$^-$ ORR catalytic cycle; f) The free energy diagram for **Belt1-4** at U=1.23 V.

kinetic diameter of O_2 is about 3.46 Å and a strong van der Waals interaction occurs at a distance of 3-6 Å.[45] The cavity size of **Belt1** (4.6 Å) is too small for O_2 to fit inside for establishing stronger interactions, thus limiting interactions to the exterior of cavity. For **Belt2-4** with larger cavity sizes, calculations revealed that O_2 adsorbs favourably within the cavities. For instance, **Belt2** (6.3 Å) in the B2S1 configuration (Figure S22) has a more suitable cavity size that allows for strong interactions with O_2, resulting in the most negative adsorption energy (ΔE_{ads} = -0.58 eV) compared to **Belt1**, **Belt3**, and **Belt4** (Figure 3a and Table S3). In **Belt2**, O_2 is centrally located, interacting with both the C3 carbon atoms (d_{vdw} = 4.69 Å) as well as the belt skeleton (d_{vdw} = 3.17 Å). However, **Belt3** (8.3 Å) and **Belt4** (11.7 Å) have cavities that are too large, leading to weaker O_2 capturing ability due to diminished interactions and a lack of confinement. These findings demonstrate that cavity size significantly influences O_2 adsorption strength and configuration.

Besides, the electron density isosurfaces of Belt**1-4** were calculated to visualize their spatial chemical environments (Figure 3b). The sp^2-skeletons of Belt**1-4** are electron-deficient due to unsaturated bonds, while the cavities and surroundings are electron-rich due to the out-of-plane radially arrayed π-electrons and nitrogen lone pair electrons. Since O_2 essentially acts as an electron acceptor, its interaction with the most electron-rich **Belt1** cavity is greatly hindered due to size restriction. As the cavity size increases in **Belt 2-4**, O_2 can be strongly adsorb into the cavities, although the centers of these belts become progressively less electron-rich due to increased distance to the π-skeletons. Moreover, the packing structures of **Belt 1-4** after O_2 adsorption are illustrated (Figure S25), revealing that O_2 molecules are sandwiched between two Belt1 molecules and reside within the cavities of other belts. In addition, the bond length of free O_2 (1.201 Å) slightly increases to 1.213, 1.233, 1.221, and 1.221 Å for **Belt1-4**, respectively, indicating pre-activation of the adsorbed O_2 with activation levels correlating to cavity sizes, which provides further insights into their ORR activity variations.

With the above analysis, we explored O_2 adsorption isotherms of **Belt1-4** under 298 K and 273 K to investigate the interactions between O_2 and belt materials (Figure 4a). Overall, **Belt2** displayed more pronounced O_2 adsorption. The isosteric

heat of adsorption per site for **Belt1-4** were estimated to be -2.54, -8.96, -5.24 and -5.31 kJ mol^{-1} (Figure 4b), respectively, using Clausius-Clapeyron equation.[46] The results indicate stronger O_2 adsorption for **Belt2**, which aligns well with the theoretical calculations. The higher affinity of O_2 to **Belt2** can be beneficial for ORR catalytic process.[47-49] The *in situ* attenuated total reflectance Fourier transform infrared spectroscopy (ATR-FTIR) was employed to gain a more comprehensive understanding of the origin and variation in the ORR catalytic activities of **Belt1-4**. In the case of **Belt 1**, no obvious peak near 1400 cm^{-1} corresponding to the *O-O vibration[50] of adsorbed O_2 can be detected in Ar and O_2 saturated 0.1 M KOH electrolyte at open circuit potential (OCP) (Figure S29a). In contrast, observable peaks for **Belt2-4** were found near 1400 cm^{-1} (Figure 4c and Figure S30a/S31a), indicating the stronger oxygen adsorption compared to **Belt1**. **Belt2** showed the most obvious oxygen absorption peak, manifesting the importance of O_2 adsorption in promoting ORR process. As the applied potential was decreased, the peak near 1400 cm^{-1} became more pronounced from 1.0 to 0.7 V (vs RHE), signifying an increase in reaction kinetics (Figure 4c). Besides, the *in situ* ATR-FTIR was also utilized to detect the possible intermediates in the ORR process. No observable change was detected near 1050 cm^{-1} (corresponding to $*O_2^-$ anion[51]) (Figure 4d and S29b/S30b/S31b), while the enhanced peak intensity near 1020 cm^{-1}, corresponding to *OOH,[52] was observed, suggesting that the first electron transfer process from O_2 to form the $*O_2^-$ anion intermediate might either not occur or proceed rapidly, leading directly to the formation of *OOH intermediate. These findings indicated the belt materials exhibited a variation in affinity to oxygen molecules in facilitating the formation of $*O_2$ intermediate, which is beneficial for ORR initiation.

It is widely accepted that the $4e^-$ reduction process from O_2 to OH^- in alkaline electrolyte generally involves diffusion and adsorption of O_2, electron transfer and protonation by H_2O to form intermediates, and dissociation of the generated OH^- ions as summarized in Table S2 (O_2 → O_2* → HOO* → O* → HO* → OH^-). Next, the adsorption energies between O_2/other involved intermediates and **Belt1-4** were calculated to identify whether the belt materials could interact differently with O_2/intermediates in any of the given steps. The results show that each intermediate (HOO, O or HO) reacted with the C3 carbon atoms (Figure S26-28), thus a plausible $4e^-$ ORR catalytic cycle was constructed based on both the experimental observations and theoretical calculations (Figure 4e). The corresponding energy diagrams of **Belt1-4** were constructed to outline their overall ORR process (Figure 4f). It can be observed that the O_2 → O_2*, HOO* → O* and O* → HO* steps are exothermic while O_2* → HOO* and HO* → OH^- are endothermic. The higher energy barrier of O_2* → HOO* indicates itself as the rate determine step in the ORR pathway. The overall energy barriers for **Belt1-4** were calculated to be 1.37, 0.86, 1.01 and 1.05 eV, respectively, which also suggests the higher activity of **Belt2** because of lower reaction initiation energy barrier.

CONCLUSION

In summary, we demonstrated that cavity-tunable carbon nanobelts with well-defined structures and precise sp^2-nitrogen doping exhibit confined interactions with O_2 in ORR electrocatalysis. Both experimental results and DFT calculations reveal that **Belt2**, with a 6.3 Å cavity, gives rise to noticeable enhancement of ORR catalytic performance, achieving high half-wave and onset potentials of 0.84 and 0.97 V, respectively. This is due to the size-induced confinement effect and the electron-rich cavity, facilitating O_2 adsorption and preactivation. As a cathode electrocatalyst in a zinc-air battery, **Belt2** also achieved a high open circuit voltage of 1.32 V and a peak power density of 181 mW cm^{-2}. This study deepens our understanding of the geometric factors affecting ORR electrocatalysis of nanocarbon materials and provides valuable insights for designing nanocarbon electrocatalysts to enhance catalytic efficiency. These findings could also contribute to advancements in other energy conversion applications and catalytic processes, such as CO_2 reduction, O_2 evolution, and N_2 reduction.

ASSOCIATED CONTENT

Supporting Information. Experimental details are included in the supporting information. Crystallographic data for **Belt1** and **Belt2** is available free of charge from the Cambridge Crystallographic Database Centre (CCDC 2053162 and 2053163).

AUTHOR INFORMATION

Corresponding Author

Jun Zhu - Institute of Materials Research and Engineering (IMRE), Agency for Science, Technology and Research

(A*STAR), 2 Fu-sionopolis Way, Singapore 138634; Orcid.org/0009-0009-9735-9151; Email: zhuj@imre.a-star.edu.sg

ACKNOWLEDGMENT

J. Z acknowledges the financial support from Singapore A*STAR MTC YIRG (M23M7c0118) and A*STAR CDF (C233312013). X. Z. acknowledges the financial support from Singapore A*STAR MTC YIRG (M23M7c0117).

REFERENCES

1. Debe, M. K. Electrocatalyst approaches and challenges for automotive fuel cells. *Nature* **2012**, *486*, 43-51.
2. Dai, L.; Xue, Y.; Qu, L.; Choi, H. J.; Baek, J. B. Metal-free catalysts for oxygen reduction reaction. *Chem. Rev.* **2015**, *115*, 4823-4892.
3. Li, Y.; Tong, Y.; Peng, F. Metal-free carbocatalysis for electrochemical oxygen reduction reaction: Activity origin and mechanism. *J. Energy Chem*. **2020**, *48*, 308-321.
4. Hu, C.; Dai, L. Carbon-Based Metal-Free Catalysts for Electrocatalysis beyond the ORR. *Agnew. Chem. Int. Ed*. **2016**, *55*, 11736-11758.
5. Liu, X.; Dai, L. Carbon-based metal-free catalysts. *Nat. Rev. Mater*. **2016**, *1*, 16064.
6. Zhang, J.; Xia, Z.; Dai, L. Carbon-based electrocatalysts for advanced energy conversion and storage. *Sci. Adv*. **2015**, *1*, e1500564.
7. Gong, K.; Du, F.; Xia, Z.; Durstock, M.; Dai, L. Nitrogen-doped carbon nanotube arrays with high electrocatalytic activity for oxygen reduction. *Science*, **2009**, *323*, 760-764.
8. Yang, L.; Jiang, S.; Zhao, Y.; Zhu, L.; Chen, S.; Wang, X.; Wu, Q.; Ma, J.; Ma, Y.; Hu, Z. Boron-doped carbon nanotubes as metal-free electrocatalysts for the oxygen reduction reaction. *Angew. Chem. Int. Ed*. **2011**, *50*, 7132-7135.
9. Qu, L.; Liu, Y.; Baek, J. -B.; Dai, L. Nitrogen-doped graphene as efficient metal-free electrocatalyst for oxygen reduction in fuel cells. *ACS Nano*, **2010**, *4*, 1321-1326.
10. Jia, Y.; Zhang, L.; Du, A.; Gao, G.; Chen, J.; Yan, X.; Brown, C. L.; Yao, X. Defect Graphene as a Trifunctional Catalyst for Electrochemical Reactions. *Adv. Mater*. **2016**, *28*, 9532-9538.
11. Liu, Z. W.; Peng, F.; Wang, H. J.; Yu, H.; Zheng, W. X.; Yang, J. Phosphorus-doped graphite layers with high electrocatalytic activity for the O2 reduction in an alkaline medium. *Angew. Chem. Int. Ed.* **2011**, *50*, 3257-3261.
12. Yang, H.; Miao, J.; Huang, S. -F.; Chen, J.; Tao, H. B.; Wang, X.; Zhang, L.; Chen, R.; Gao, J.; Chen, H.; Dai, L.; Liu, B. Identification of catalytic sites for oxygen reduction and oxygen evolution in N-doped graphene materials: Development of highly efficient metal-free bifunctional electrocatalyst. *Sci. Adv*. **2016**, *2*, e1501122.
13. Wu, Y.; Li, C.; Liu, W.; Li, H.; Gong, Y.; Niu, L.; Liu, X.; Sun, C.; Xu, S. Unexpected monoatomic catalytic-host synergetic OER/ORR by graphitic carbon nitride: density functional theory. *Nanoscale* **2019***, 11*, 5064-5071.
14. Li, D.; Li, C.; Zhang, L.; Li, H.; Zhu, L.; Yang, D.; Fang, Q.; Qiu, S.; Yao, X. Metal-free thiophene-sulfur covalent organic frameworks: precise and controllable synthesis of catalytic active sites for oxygen reduction. *J. Am. Chem. Soc*. **2020**, *142*, 8104-8108.
15. Yue, J. Y.; Wang, Y. T.; Wu, X.; Yang, P.; Ma, Y.; Liu, X. H.; Tang, B. Two-dimensional porphyrin covalent organic frameworks with tunable catalytic active sites for the oxygen reduction reaction. *Chem. Commun*. (Camb) **2021**, *57*, 12619-12622.
16. Cui, X.; Lei, S.; Wang, A. C.; Gao, L.; Zhang, Q.; Yang, Y.; Lin, Z. Emerging covalent organic frameworks tailored materials for electrocatalysis. *Nano. Energy*. **2020**, 70, 104525.
17. Chen, G.; Zhong, H.; Feng, X. Active site engineering of single-atom carbonaceous electrocatalysts for the oxygen reduction reaction. *Chem. Sci*. **2021**, *12*, 15802-15820.
18. Sharifi, T.; Gracia-Espino, E.; Chen, A.; Hu, G.; Wågberg, T. Oxygen reduction reactions on single- or few-atom discrete active sites for heterogeneous catalysis. *Adv. Energy Mater*. **2019**, *10*, 1902084.
19. Chen, H.; Liang, X.; Liu, Y.; Ai, X.; Asefa, T.; Zou, X. Active site engineering in porous electrocatalysts. *Adv. Mater*. **2020**, *32*, e2002435.
20. Tang, L.; Meng, X.; Deng, D.; Bao, X. Confinement catalysis with 2D materials for energy conversion. *Adv. Mater*. **2019**, *31*, e1901996.
21. Wordsworth, J.; Benedetti, T. M.; Somerville, S. V.; Schuhmann, W.; Tilley, R. D.; Gooding, J. J. The influence of nanoconfinement on electrocatalysis. *Angew. Chem. Int. Ed*. **2022**, *61*, e202200755.
22. Avid, A.; Zenyuk, I. V. Confinement effects for nano-electrocatalysts for oxygen reduction reaction. *Curr. Opin. Electrochem*. **2021**, *25*, 100634.
23. Yang, F.; Deng, D.; Pan, X.; Fu, Q.; Bao, X. Understanding nano effects in catalysis. *Natl. Sci. Rev*. **2015**, *2*, 183-201.
24. Dai, H. Carbon nanotubes: opportunities and challenges *Surf. Sci*. **2022**, *500*, 218-241.
25. He, Q.; Qiao, S.; Zhou, Y.; Vajtai, R.; Li, D.; Ajayan, P. M.; Ci, L.; Song, L. Carbon nanotubes-based electrocatalysts: structural regulation, support effect, and synchrotron-based characterization. *Adv. Funct. Mater*. **2021**, *32*, 2106684.
26. Fujigaya, T.; Nakashima, N. Fuel cell electrocatalyst using polybenzimidazole-modified carbon nanotubes as support materials. *Adv. Mater*. **2013**, *25*, 1666-1681, 201204461.
27. Agui, L.; Yanez-Sedeno, P.; Pingarron, J. M. Role of carbon nanotubes in electroanalytical chemistry: a review. *Anal. Chim. Acta*. **2008**, *622*, 11-47.
28. Yang, L.; Zhao, Y.; Chen, S.; Wu, Q.; Wang, X.; Hu, Z. A mini review on carbon-based metal-free electrocatalysts for oxygen reduction reaction. *Chinese J. of Catal*. **2013**, *34*, 1986-1991.
29. Wang, D.-W.; Su, D. Heterogeneous nanocarbon materials for oxygen reduction reaction. *Energy Environ. Sci*. **2014**, *7*, 576-591.
30. Zhang, Y.; Jiao, Y.; Jaroniec, M.; Jin, Y.; Qiao, S. Nanostructured metal-free electrochemical catalysts for highly efficient oxygen reduction. *Small* **2012**, *8*, 3550-3566.
31. Mabena, L. F.; Sinha Ray, S.; Mhlanga, S. D.; Coville, N. J. Nitrogen-doped carbon nanotubes as a metal catalyst support. *Appl. Nanosci*. **2011**, *1*, 67-77.
32. Wei, Q.; Tong, X.; Zhang, G.; Qiao, J.; Gong, Q.; Sun, S. Nitrogen-doped carbon nanotube and graphene materials for oxygen reduction reactions. *Catalysts* **2015**, *5*, 1574-1602.
33. Singh, S. K.; Takeyasu, K.; Nakamura, J. Active sites and mechanism of oxygen reduction reaction electrocatalysis on nitrogen-doped carbon materials. *Adv. Mater*. **2019**, *31*, e1804297.
34. Segawa, Y.; Yagi, A.; Matsui, K.; Itami, K. Design and synthesis of carbon nanotube segments. *Angew. Chem. Int. Ed*. **2016**, *55*, 5136-5158.
35. Povie, G.; Segawa, Y.; Nishihara, T.; Miyauchi, Y.; Itami, K. Synthesis of a carbon nanobelt. *Science*, **2017**, *356*, 172-175.
36. Hermann, M.; Wassy, D.; Esser, B. Conjugated nanohoops incorporating donor, acceptor, hetero- or polycyclic aromatics. *Angew. Chem. Int. Ed*. **2021**, *60*, 15743-15766.
37. Zhu, J.; Han, Y.; Ni, Y.; Li, G.; Wu, J. Facile synthesis of nitrogen-doped [(6.)m8]n cyclacene carbon nanobelts by a one-pot self-condensation reaction. *J. Am. Chem. Soc*. **2021**, *143*, 2716-2721.
38. Zhu, J.; Han, Y.; Ni, Y.; Wu, S.; Zhang, Q.; Jiao, T.; Li, Z.; Wu, J. Facile synthesis of a fully fused, three-dimensional pi-conjugated archimedean cage with magnetically shielded cavity. *J. Am. Chem. Soc*. **2021**, *143*, 14314-14321.
39. Paudler, W. W.; Zeiler, A. G. The Synthesis of dibenzo[b,f][l,5]diazocine. *Chem. Commun*. (London), **1967**, *21*, 1077-1078.

40. Guo, D.; Shibuya, R.; Akiba, C.; Saji, S.; Kondo, T. Active sites of nitrogen-doped carbon materials for oxygen reduction reaction clarified using model catalysts. J. Nakamura, *Science*, **2016**, *351*, 361-365.
41. Singh, S. K.; Takeyasu, K.; Nakamura, J. Active sites and mechanism of oxygen reduction reaction electrocatalysis on nitrogen-doped carbon materials. *Adv. Mater*. **2019**, *31*, e1804297.
42. Hu, X.; Wu, Y.; Li, H.; Zhang, Z. Adsorption and Activation of O2 on Nitrogen-Doped Carbon Nanotubes. *J. Phys. Chem. C*, **2010**, *114*, 9603–9607.
43. Chen, X.; Hu, R.; Bai, F. DFT study of the oxygen reduction reaction activity on Fe-N(4)-patched carbon nanotubes: the influence of the diameter and length. *Materials* (Basel) **2017**, *10*, 549.
44. Ghasemy, E.; Motejadded, H. B.; rashidi, A.; Hamzehlouyan, T.; Yousefian, Z. N-doped CNT nanocatalyst prepared from camphor and urea for gas phase desulfurization: experimental and DFT study. *J. of Taiwan Inst. of Chem. E*. **2018**, *85*, 121-131.
45. Sutton, A. L.; Melag, L.; Sadiq, M. M.; Hill, M. R. Capture, storage, and release of oxygen by metal-organic frameworks (MOFs). *Angew. Chem. Int. Ed*. **2022**, *61*, e202208305.
46. Wark, Kenneth, **1988**. "Generalized Thermodynamic Relationships". Thermodynamics (5th ed.). New York, NY: McGraw-Hill, *Inc*. ISBN 978-0-07-068286-3.
47. Yin, W. W.; Wan Daud, W. R.; Mohamad, A. B.; Kadhum, A. A. H.; Shyuan, L. K.; Majlan, E. H. Density-functional theory of O_2 physical adsorption on sp^3 and sp^2 hybridized nitrogen-doped CNT surfaces for fuel cell electrode. *Adv. Mater. Res*. **2011**, *233-235*, 17-22.
48. de Falco, G.; Florent, M.; Jagiello, J.; Cheng, Y.; Daemen, L. L.; Ramirez-Cuesta, A. J.; Bandosz, T. J. Alternative view of oxygen reduction on porous carbon electrocatalysts: the substance of complex oxygen-surface interactions. *iScience* **2021**, *24*, 102216.
49. Wang, S.; Yu, D.; Dai, L., Polyelectrolyte functionalized carbon nanotubes as efficient metal-free electrocatalysts for oxygen reduction. *J. Am. Chem. Soc*. **2011**, *133*, 5182-5185.
50. Kunimatsu, K.; Yoda, T.; Tryk, D. A.; Uchida, H.; Watanabe, M. In situ ATR-FTIR study of oxygen reduction at the Pt/Nafion interface. *Phys. Chem. Chem. Phys*. **2010**, *12*, 621-629.
51. Cheng, W.; Zhao, X.; Su, H.; Tang, F.; Che, W.; Zhang, H.; Liu, Q. Lattice-strained metal–organic-framework arrays for bifunctional oxygen electrocatalysis. *Nat. Energy* **2019**, *4*, 115-122.
52. Zhang, M.; de Respinis, M.; Frei, H. Time-resolved observations of water oxidation intermediates on a cobalt oxide nanoparticle catalyst. *Nat. Chem*. **2014**, *6*, 362-367.

Graphic entry for the Table of Contents

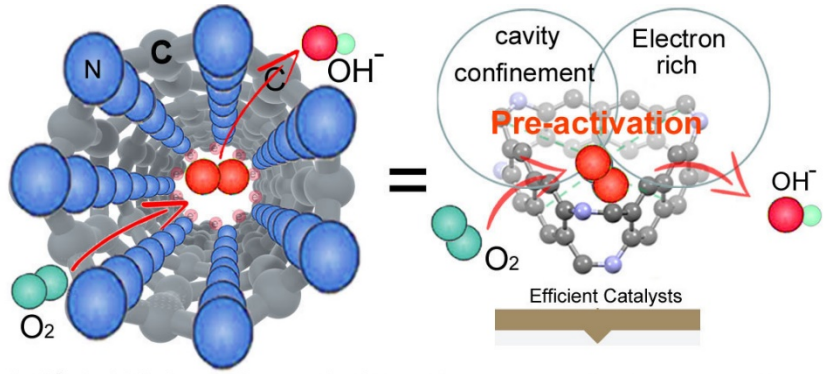

Artificial N doped nanobelts Oxygen reduction reaction